Chapter 2

ARRAY-LEVEL INVERSE DESIGN OF ACTIVE METASURFACES FOR OPTIMIZED SPATIAL WAVEFRONTS

The material in this chapter was in part presented in [46].

2.1 Beam steering with optical metasurfaces

Optical beam steering has become a major focus of global research owing to its significance in technologies such as light detection and ranging (LiDAR), free space optical communications, and holographic displays [47–50]. Operating at near-infrared (NIR) and visible wavelengths offers the potential to enable high-resolution beam steering with reduced footprints compared to radiofrequeny (RF) phased arrays.

Beam steering is achieved by precisely controlling the phase and amplitude of light emitted or scattered from each antenna in an array, leading to constructive interference in a desired direction. In passive metasurfaces, this control is typically achieved by designing individual resonators that impart abrupt phase changes in light scattered at an interface while maintaining constant amplitude. By arranging these resonators to create constant spatial phase gradients, researchers have demonstrated effects such as anomalous refraction or reflection [23, 27, 51, 52]. The angles of refraction (θ_t) and reflection (θ_r) are determined by the design-specific phase gradient $\frac{d\Phi}{dx}$, as described by the generalized Snell's law [51]:

$$\begin{aligned} \sin(\theta_t)n_t - \sin(\theta_i)n_i &= \frac{\lambda_0}{2\pi}\frac{d\Phi}{dx} \\ \sin(\theta_r) - \sin(\theta_i) &= \frac{\lambda_0}{2\pi n_i}\frac{d\Phi}{dx}. \end{aligned} \tag{2.1}$$

Here, n_t and n_i are the refractive indices of the media in which light is transmitted and incident, respectively, and λ_0 is the vacuum wavelength. The design of these phase gradient arrays can be understood as a *forward* design process that results in anomalous refraction or reflection at a single, design-specific angle. However, the lack of post-fabrication tunability in passive metasurfaces limits their applicability in practical scenarios.

Active metasurfaces address the limitations of their passive counterparts by integrating a tunable permittivity layer that enables dynamic changes in the refractive index in response to an external stimulus, such as a bias voltage. To achieve a wide range of amplitude and phase values, reconfigurable optical frequency metasurfaces generally rely on intrinsic material and geometric resonances. This approach introduces nonidealities in the optical response. Unlike passive structures, active metasurfaces often exhibit a strongly covarying phase and amplitude as function of the applied bias. Additionally, it is challenging to design tunable permittivity antennas with a full phase modulation range of 360° [53, 54]. As a result, active beam steering metasurfaces with forward-designed array phase profiles result in decreased directivities due to significant power coupling into undesired sidelobes [42].

In this chapter, we introduce an array-level *inverse* design approach as a solution to optimize the spatial bias configuration across an array considering the nonideal antenna amplitude and phase response. Previously, inverse design techniques have been applied to shape and topology optimization of individual nanophotonic components, such as antennas in passive metasurfaces [55–59]. These methods involve iteratively adjusting the shape and size of each nanoantenna until the desired optical response is achieved. Various methods including the adjoint variable method [55, 60], genetic algorithms [58, 61], and machine learning [60, 62, 63] have been successfully used for this purpose.

For active metasurfaces, an analogous approach starts with designing an array of geometrically identical nanoantennas that exhibit optimal phase and amplitude tunability in response to an external control variable. Thus, the critical component-level inverse design objective shifts from optimizing the shape of a passive metasurface element to engineering nanoantennas with optimal functional characteristics, such as the range of achievable amplitude, phase, or polarization values in response to its inputs. Once an optimal active antenna design is developed, the scattering properties of the entire array can be co-optimized to meet a specific performance objective. Due to the added complexity of this process, the inverse design of active metasurfaces has remained largely unexplored until recently.

Chung *et al.* [64] demonstrated inverse design of an active beam switching metasurface. Notably, the liquid crystal-based metasurface considered in this work operated in only two states: voltage on and off. As a consequence, topology optimization of individual unit cells was required to facilitate beam switching between different diffraction orders. In contrast, the array-level inverse design approach outlined here leverages the tunability of individual active nanoantennas that is made possible by applying an independent bias to each metasurface antenna. This approach results in an array of active antennas, each with continuously variable phase and amplitude, yielding a vast number of operational states that enable versatile metasurface function. Consequently, the phase and amplitude of scattered light can be optimized across a large array without any change in the geometric configuration of individual components.

In the following sections, we discuss conventional approaches for forward designs of ideal antenna arrays and the limitations encountered with nonideal, realistic active metasurface designs. We utilize a genetic algorithm for an iterative optimization of a figure of merit (FOM) that analytically models the desired function of a metasurface with uncoupled antennas. Further, we assess the robustness of the optimized designs through numerical studies, examining the effects of inaccuracies in the applied voltages and evaluating the impact of amplitude and phase modulation on the achievable performance. Finally, we experimentally validate our approach using a plasmonic indium tin oxide (ITO)-based field-effect tunable metasurface and discuss the realization of more advanced metasurface functions, such as the creation of flat-top beams, variable beam widths, and simultaneous steering of multiple beams.

2.2 Forward design of ideal antenna arrays

The electric far-field E_{ff} of an array of scatterers is calculated by pattern multiplication of the electric far-field of a unit cell E_{antenna} with the array factor. This calculation is based on antenna array theory [65, 66], which was initially developed for RF phased arrays. As RF phased arrays can maintain large interantenna spacings without the introduction of additional diffraction orders, their far-field response can be modeled as that of an array of independent scatterers with negligible near-field coupling. The far-field response is thus obtained by applying the Fraunhofer approximation to the superposition of individual electric field contributions from each scattering element.

This assumption becomes non-trivial in the case of optical metasurfaces with subwavelength antenna spacings, as the characteristic period d_x between neighboring antennas approaches the electromagnetic near-field regime given by $2d_x/\lambda^2$. Thus, coupling between neighboring elements can only be neglected for antennas that are spaced at large enough distances and/or possess strongly confined modes. The validity of this assumption should be verified for each metasurface design through analysis of the electromagnetic near-field, or by comparing the calculated far-field profile to results obtained for full-wave simulations of an antenna array with spatially varying bias configurations.

For one-dimensional (1D) arrays, as the ones considered in the following study, the array factor is computed by taking into account the phase φ_n, amplitude A_n, as well as the period d_x that defines the position of the n-th antenna element (Fig. 2.1a). The scattered light phase and amplitude are determined by the external stimulus applied to each antenna, such as a bias voltage V_n. The electric far-field E_{ff} can then be written as

$$E_{\mathrm{ff}}(\theta) = E_{\mathrm{antenna}}(\theta) \cdot \sum_n \left[A_n(V_n) \exp\big(i\varphi_n(V_n)\big) \exp\big(ik(n-1)d_x \sin(\theta)\big) \right]. \quad (2.2)$$

Here, θ is the polar angle, and $k = 2\pi/\lambda$ is the wavenumber associated with the operating wavelength λ. A 1D configuration of a square antenna array is realized by connecting antennas along one axis and enabling independent control of each element in the perpendicular direction (Fig. 2.1b). In a beam steering reflectarray, the incident light is normal to the metasurface, and the reflected beam is steered at a desired angle θ_{r}.

We define an ideal antenna response as one that yields a constant unit amplitude and a smoothly varying phase with a 360° phase modulation range (Fig. 2.1c). The respective ideal amplitude and phase properties are commonly reported in conventional phased array systems [5] as well as passive metasurfaces [51], and facilitate intuitively understandable forward design of phase gradient profiles for highly directive beam steering with minimal power loss in sidelobes. The additional manifestation of unit amplitude at each antenna element results in maximal power efficiency.

Figure 2.1d illustrates a forward-designed phase gradient profile with a constant phase shift φ_s between adjacent antennas in an ideal reflectarray. The array consists of 100 antennas that are uniformly arranged at a spacing of $d_x = 400$ nm. The operating wavelength is $\lambda = 1550$ nm. For an incident beam normal to the array, φ_s is computed as

$$\varphi_s = 360° \cdot \frac{d_x \sin(\theta_{\mathrm{r}})}{\lambda}. \quad (2.3)$$

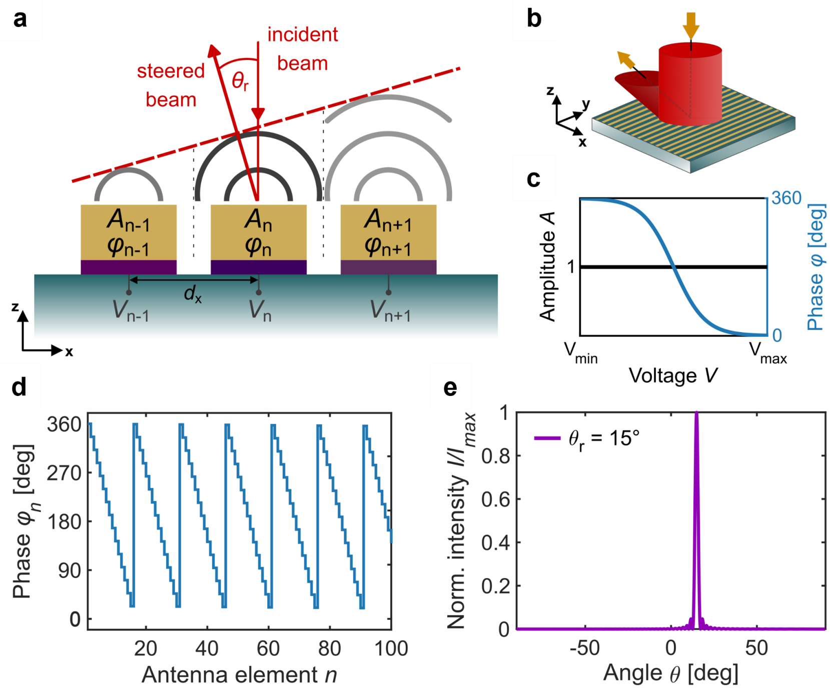

Figure 2.1: **Beam steering with ideal antenna array**. (a) Schematic of beam steering active metasurface: application of voltage stimulus V_n on antenna n (yellow) alters the complex dielectric permittivity of the active layer, indicated in shades of violet. As a consequence, the scattered light amplitude and phase of element n, A_n and ϕ_n, respectively, are varied. The antennas are arranged uniformly at a period d_x. We consider a reflectarray with incident light normal to the surface. Beam steering is achieved through constructive interference of the scattered light at the desired steering angle θ_r. (b) Schematic of a one-dimensional tunable metasurface. Antennas are connected in y-direction and allow independent control in x. (c) Representative scattered light amplitude and phase response on an ideal active antenna array for applied bias voltages from V_{min} to V_{max}. (d) Forward design of phase gradient profile for an ideal phased array consisting of 100 antennas arranged at a period of $d_x = 400$ nm. The operating wavelength is $\lambda = 1550$ nm and the target steering angle is $\theta_r = 15°$. (e) Normalized far-field intensity I/I_{max} *vs* polar angle θ for spatial phase profile shown in (d) with constant amplitude.

Wrapping of the phase profiles around 360° allows the design of blazed grating-like structures that steer the reflected beam in the desired direction. Due to a discrete sampling of the phases at fixed spatial increments d_x, the blazed grating of an antenna array comprises of discontinuous steps. The discrete sampling furthermore results in an aperiodicity of the phase profiles over the entire array, as a complete phase shift of 360° is not necessarily an integer multiple of φ_s. The phase profiles approach periodic blazed gratings for all steering angles as d_x approaches smaller values.

Assuming constant amplitude, the phase gradient profile shown in Fig. 2.1d results in a directive beam steered at $\theta_r = 15°$ with minimal power scattered in other directions (Fig. 2.1e). The far-field radiation pattern is calculated as $I(\theta) = |E_{\mathrm{ff}}(\theta)|^2$. Individual antennas are approximated as omnidirectional scattering elements with $E_{\mathrm{antenna}}(\theta) = 1$. For the purpose of our study, we quantify the beam steering performance of the array by the directivity, defined as the ratio between the intensity at the desired angle θ_r to the power radiated in all directions normalized by the solid angle (Eq. 2.4). In contrast to efficiency, directivity remains unaffected by scaling of the far-field radiation pattern by a constant factor. For a one-dimensional reflectarray radiating into a half-space, the directivity $D(\theta_\mathrm{r})$ is formalized as [65]

$$D(\theta_\mathrm{r}) = \frac{\pi \cdot I(\theta_\mathrm{r})}{\int_{-\pi/2}^{\pi/2} I(\theta)\mathrm{d}\theta}. \tag{2.4}$$

For the ideal structure showcased in Fig. 2.1, equation 2.4 yields a directivity of $D_{\mathrm{ideal}} = 78.2$. The sidelobe level SL is proportional to the ratio of the second largest to largest peak intensity, $I_{\mathrm{max,2}}$ and I_{max}, respectively,

$$\mathrm{SL} = 10\log_{10}\left(\frac{I_{\mathrm{max,2}}}{I_{\mathrm{max}}}\right) \tag{2.5}$$

and corresponds to $\mathrm{SL}_{\mathrm{ideal}} = -13.3$ dB.

2.3 Nonideal active metasurfaces: Forward and array-level inverse design

Forward design

In contrast to ideal phased arrays, active metasurfaces typically exhibit a nonideal optical response due to the device-specific modulation mechanism. Here, we illustrate this behavior using the example of a field-effect tunable, plasmonic metasurface introduced in [42]. Figure 2.2a shows a square unit cell with a characteristic period of $d_x = 400$ nm. It consists of a rectangular gold (Au) patch over a hafnium oxide/aluminum oxide laminated (HfO_2/Al_2O_3, or HAOL) gate dielectric and an active ITO layer. This composite structure is deposited on top of an Al_2O_3 dielectric spacer and an Au back reflector. Au electrodes intersecting the top metal patches in the y-direction enable the formation of equipotential rows, analogous to the 1D beam steering array shown in Fig. 2.1b. The entire metasurface consists of 96 independently addressable rows, referred to as metasurface antennas.

Active control is achieved by employing field-effect induced changes in refractive index to modulate the scattered light properties [67, 68]. Upon application of a bias voltage between the ITO and the top Au antenna, the reflectance and phase response are modulated as illustrated in Fig. 2.2b for an operating wavelength of $\lambda = 1510$ nm. This modulation occurs due to the Au-HAOL-ITO heterostructure, which functions as a metal-oxide-semiconductor (MOS) capacitor. Application of an electrical bias between the Au electrode and the ITO layer introduces a carrier density modulation in the ITO. Thus, a change in the complex dielectric permittivity of the ITO, ε_{ITO}, occurs in a thin layer at the interface to the gate dielectric [53], as described by the Drude model. Upon alteration of the applied electric field, $\text{Re}(\varepsilon_{\text{ITO}})$ switches its sign from positive to negative, undergoing an epsilon-near-zero (ENZ) transition, as highlighted in Fig. 2.2c with the gray shaded region. The continuity of the normal electric displacement component at the interface between two media requires

$$\varepsilon_1 \cdot E_{1\perp} = \varepsilon_2 \cdot E_{2\perp} \tag{2.6}$$

where ε_i is the complex dielectric permittivity and $E_{i\perp}$ is the normal electric field component in medium i. Hence, operation at an ENZ condition results in a strong field enhancement in the active ITO layer [30]. Spectral overlap of the ENZ transition with the magnetic dipole resonance of the antenna ensures a strong modulation of the scattered light response, allowing for reconfigurable device operation at telecommunication wavelengths. We note here that while $\text{Re}(\varepsilon_{\text{ITO}})$ is required to go to zero to satisfy the ENZ condition and ensure a large phase modulation, $\text{Im}(\varepsilon_{\text{ITO}})$ takes nonzero values (Fig. 2.2d). These losses, emerging from absorption in the active layer due to electron-electron collisions [69], result in reduced scattered light amplitudes.

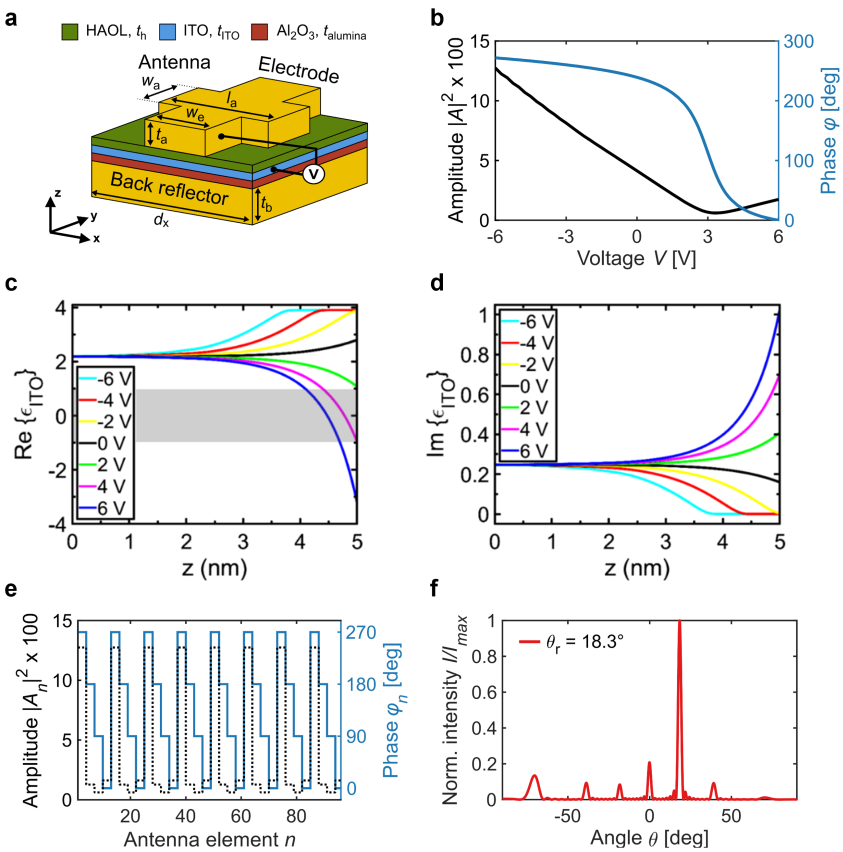

Figure 2.2: **Beam steering with nonideal plasmonic field-effect tunable metasurface.** (a) Square unit cell of active metasurface as introduced in [42]. Constitutive layers from top to bottom: Au rectangular patch (t_a = 40 nm, w_a = 130 nm, l_a = 230 nm) and electrode (w_e = 150 nm), HAOL dielectric spacer (t_h = 9.5 nm), active ITO layer (t_{ITO} = 5 nm), Al_2O_3 dielectric layer ($t_{alumina}$ = 9.5 nm), and Au back reflector (t_b = 80 nm). The metasurface consists of individually addressable antennas in x which are periodically arranged at a spacing of d_x = 400 nm. (b) Scattered light amplitude (black) and acquired phase (blue) response as function of applied bias voltage at λ = 1510 nm. For clarity, the phase axis is set to 0° at its minimal value. The optical properties are obtained through full-wave simulations (Lumerical FDTD) of a periodic array of the unit cell with a given bias voltage across the entire array. (c) Real and (d) imaginary part of the ITO permittivity as function of z-position for different applied bias voltages at λ = 1510 nm. The gray-shaded region in (c) shows the ENZ regime where $-1 < \mathrm{Re}\{\varepsilon_{ITO}\} < +1$. z = 5 nm denotes the interface of the ITO and the HAOL gate dielectric, z = 0 nm represents the interface of the ITO and the Al_2O_3 dielectric layer, as indicated in the inset of (d). (e) Stairstep phase (blue) and amplitude (black dotted) profile for steering at θ_r = 18.3°. (f) Normalized far-field intensity I/I_{max} as function of polar angle θ for forward design shown in (e).

Generally, the operation wavelength is chosen so as to give rise to large phase modulation with a modest change in amplitude [42]. Nevertheless, the active metasurface exhibits a nonideal optical response (Fig. 2.2b) with (i) a nonunity amplitude, (ii) a limited phase modulation range of 272°, and (iii) covariation of the scattered light amplitude and phase properties with applied bias. These nonidealities significantly limit the beam steering performance of such a metasurface array designed using forward approach in the following ways: First, reduced phase modulation requires adjustment to ideal blazed grating designs. Stairstep phase profiles approximate the spatial phase gradients, as shown in Fig. 2.2e [42]. A dynamic change of the repetition number (*i.e.*, number of adjacent antennas with the same phase value) results in beam steering at a set of discrete angles. However, a reduced phase modulation introduces increased number of sidelobes in the far-field radiation pattern. Moreover, the additional covariance of the scattered light amplitude and phase rules out the design of pure phase gratings. Since an intuition-based forward design does not account for amplitude-phase covariation, substantial power is coupled into undesired sidelobes, as shown in Fig. 2.2f for steering at an angle of $\theta_\mathrm{r} = 18.3°$. As a result of these nonidealities, we observe a significant drop in directivity to $D_\mathrm{forward} = 39.5$ with a sidelobe level of $\mathrm{SL}_\mathrm{forward} = -6.8$ dB.

The radiation pattern shown in Fig. 2.2f is obtained using the array factor calculation (Eq. 2.2) for an array of independent antennas. We verify the validity of this approach by comparing the analytically calculated radiation patterns to full-wave simulations [42] for forward-designed array profiles. Two apparent effects are observed in Fig. 2.3: Firstly, rather than an increase in the relative magnitude of the sidelobes, which would indicate interantenna coupling, Fig. 2.3a-c depict an attenuation of the sidelobes at broadside angles in the simulated radiation patterns. This effect increases the simulated directivity D_sim in comparison to its analytically computed counterpart D_AF that is based on array factor calculations. Secondly, a strong increase in the relative magnitude of the zero-order sidelobe and thus decrease in D_sim is reported for $\theta_\mathrm{r} = 70.7°$ (Fig. 2.3d). To understand the observed deviations, we remind ourselves that the analytical calculations are performed for omnidirectional scatterers with $E_\mathrm{antenna} = 1$. While this assumption is valid for a broad range of steering angles with the current nanoantenna design, it breaks down at larger angles. Nonetheless, due to the validity of the analytically computed radiation pattern for a wide range of steering angles, no appearance of additional sidelobes, and a good match between the computed directivities for the simulated and analytically obtained radiation patterns (Fig. 2.3), we can use the array factor calculation to develop new design strategies for optimized beam steering with nonideal antennas.

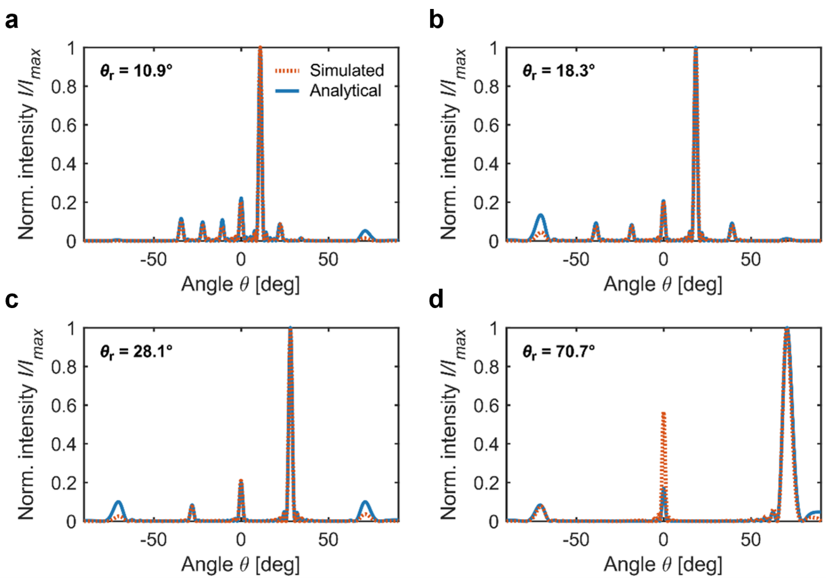

Figure 2.3: **Comparison of far-field radiation patterns obtained through full-wave simulations and analytical array factor calculations.** Normalized far-field intensity I/I_{max} for full-wave simulations [42] (orange dashed) and analytical array factor calculations (blue). The results are obtained using forward-designed stairstep array profiles for an array of 96 antennas arranged at a period of d_{x} = 400 nm and at a wavelength of λ = 1510 nm. The simulated (D_{sim}) and analytically calculated (D_{AF}) directivities at the respective steering angles θ_{r} are (a) D_{sim} = 51.0 and D_{AF} = 43.5, (b) D_{sim} = 48.3 and D_{AF} = 39.5, (c) D_{sim} = 50.1 and D_{AF} = 39.1, (d) D_{sim} = 22.2 and D_{AF} = 23.0.

Array-level inverse design

Here, we report an array-level inverse design algorithm that computes the bias voltage configuration for an electrically tunable metasurface to achieve optimized beam steering. Since each metasurfaces antenna is gated individually, the algorithm aims to optimize the covarying phase and amplitude value at each antenna. We address this multiparameter, global optimization problem using genetic algorithms (GA). In contrast to local search methods, genetic algorithms are based on stochastic optimizers that can escape local optima [70, 71]. In addition, they are highly suitable for discrete solution domains with discontinuous or nondifferentiable objective functions [59]. An inherently high-dimensional solution space arises due to simultaneous optimization of 96 metasurface antennas. This challenge is overcome by implementing an iterative genetic optimization that relies on a gradual increase of the solution space. The algorithm initially runs an optimization for a reduced number of consecutive antennas, which are periodically repeated over the entire array. Once an optimal solution is found, it is provided to the next bigger solution domain as an initial solution. The final iteration simultaneously optimizes all variables. This approach enables the algorithm to effectively find near-optimal solutions in high-dimensional optimization spaces, while maintaining all degrees of freedom. Due to the stochastic nature of genetic optimization, the algorithm is run multiple times to obtain the optimal result in an extended data set. Further details on the implementation of the iterative genetic optimization algorithm, the distribution and robustness of the optimized results, and a comparison to alternative genetic optimization approaches are provided in Section A.1 of the Appendix. We would like to highlight that due the high dimensionality of the nonconvex solution space given in this problem, the search for an absolute global optimum becomes infeasible. Thus, we compare the optimized FOM to the corresponding performance measure of an ideal antenna array in order to assess its proximity to a desired reference value.

The beam steering optimization consists of maximizing the directivity at the desired steering angle θ_r. Thus, the objective function is defined as

$$\mathrm{FOM}(\theta_r, \varphi_n(V_n), A_n(V_n)) = D(\theta_r). \tag{2.7}$$

The directivity accounts for the antenna-specific control variables (in this case, bias voltage) to maximize the intensity at θ_r, while minimizing power scattered in all other directions. The latter also simultaneously minimizes beam divergence, which is quantified by the full width at half-maximum (FWHM) of the steered beam. The inverse design algorithm outputs a highly nonintuitive array phase profile, as shown in Fig. 2.4a for the same steering angle of $\theta_r = 18.3°$. The seemingly periodic nature of the spatial phase profile arises from the phase gradient required to steer a beam at a specified angle as well as the iterative design approach. Since the inverse design optimizes the covarying phase and amplitude values at each antenna, the algorithm aims to minimize the amplitude modulation A_{mod} over the entire antenna array.

$$A_{mod} = \frac{|A_{max}|^2 - |A_{min}|^2}{|A_{min}|^2}. \tag{2.8}$$

Here, A_{max} and A_{min} correspond to the maximal and minimal amplitudes, respectively. The amplitude modulation for the forward-designed array profile (Fig. 2.2e) corresponds to $A_{\text{mod,forward}} = 19.7$. In comparison, the amplitude modulation using the inverse design approach (Fig. 2.4a) is $A_{\text{mod,inverse}} = 11.8$. As a result, by accounting for the antenna-specific scattered light properties, the co-optimization of phase and amplitude at each each antenna results in significant sidelobe suppression, as shown in Fig. 2.4b. The optimized directivity for steering at $\theta_r = 18.3°$ is $D_{\text{inverse}} = 72.7$, representing a substantial increase of 84% compared to the previously demonstrated forward design with $D_{\text{forward}} = 39.5$. Similarly, the sidelobe level obtained through inverse design amounts to $\text{SL}_{\text{inverse}} = -13.2$ dB.

These findings highlight the ability of the optimized radiation patterns to approach ideal beam steering. The approach was further generalized to the case of beam steering at angular increments of 0.5°. Figure 2.4c shows a comparison of the directivity values obtained with forward and inverse design, respectively. The results highlight the ability of optimized designs in a nonideal antenna array to approach the performance of an ideal phased array (dashed) at all steering angles. This contrasts with the results of forward design, where we evaluate the previously introduced stairstep phase profiles for steering at a discrete set of angles as well as linear phase profiles. Linear phase profiles are those that are truncated symmetrically to remain within the restricted phase modulation range. This method offers an alternative approach to achieve continuous beam steering with limited phase modulation using forward design. As both approaches do not account for the nonideal optical response of the metasurface, reduced performance is observed using the forward design approach.

The cosine-like decrease of directivity with increasing steering angles can be understood by considering the two limiting factors defining beam directivity: the magnitude of the sidelobes relative to the peak intensity at θ_r (*i.e.*, the sidelobe level SL), and the FWHM of the main lobe. Notably, the prior does not change monotonically as the beam is scanned over the half space and remains around a constant value (inset of Fig. 2.4d). Thus, the decrease in directivity is attributed to the diminished effect of aperture size at oblique angles. That is, the antenna array aperture appears to be reduced in size at larger steering angles, leading to a broadening of the beam, as illustrated in Fig. 2.4d. Furthermore, since the reflectarray configuration does not allow for radiation to go beyond 90°, the main lobe is truncated for angles greater than 80°. Thus, an increase in directivity and a simultaneous decrease in FWHM is reported for the corresponding steering range.

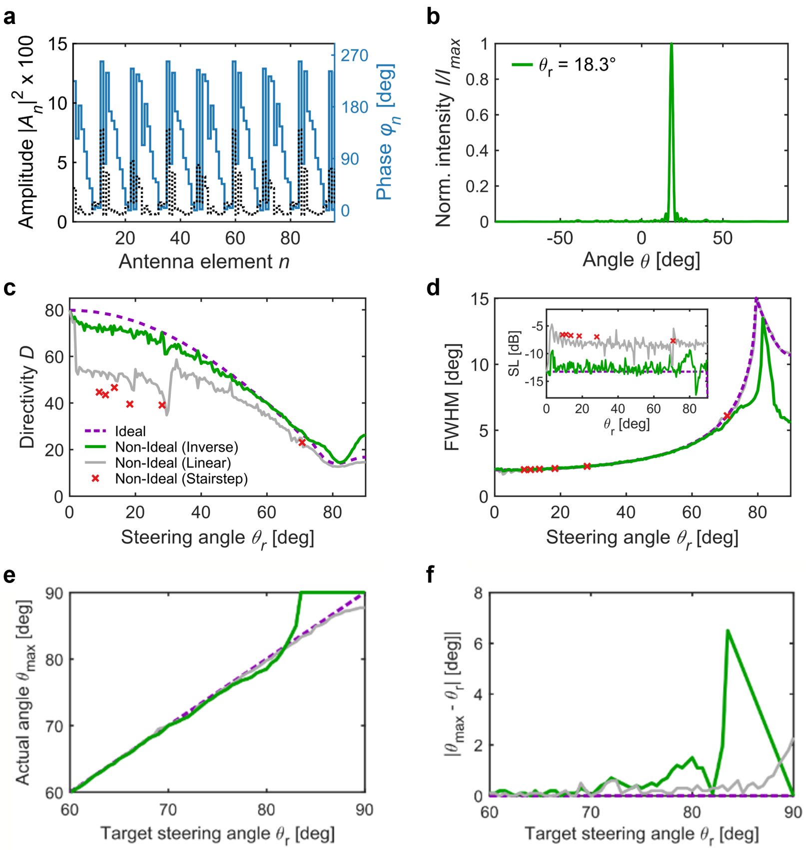

Figure 2.4: **Beam steering of nonideal active metasurface with array-level inverse design.** (a) Optimized phase profile (blue) with corresponding amplitude profile (black dotted) generated by inverse design for steering at $\theta_r = 18.3°$. (b) Normalized far-field intensity I/I_{max} *vs* polar angle θ for inverse-designed active metasurface. (c) Optimized directivity (green) for beam steering angles θ_r ranging from 0° to 90° at angular increments of 0.5°. The beam directivity (c) and sidelobe level (d) for ideal (dashed violet), forward designs consisting of linear truncated (gray), and stairstep (red crossed) phase profiles are shown for comparison. All results are obtained for the active metasurface introduced in Fig. 2.2. The aperture of the metasurface is 38.4 μm.

An evaluation of the difference between the actual and target steering angle shows that the target steering angle is achieved with $\leq 0.2°$ absolute deviation for steering angles up to 70°. For broadside angles, this value increases as steering in nonuniform angular increments is observed due to the limited phase modulation (Fig. 2.4e). Since a directivity optimization entails maximizing the intensity at θ_r while minimizing the beam divergence and sidelobes, inverse design can enhance the directivity at broadside angles by reducing the FWHM even when the actual steering angle θ_{max} does not correspond to θ_r. Figures 2.4e and f illustrate how θ_{max} and the absolute deviation from the desired steering angle $|\theta_{max} - \theta_r|$ evolve for forward- and inverse-designed arrays. Additional constraints can be implemented in the algorithm to improve the accuracy of the steered beam across all desired steering angles.

2.4 Impact of phase and amplitude modulation

A seemingly fundamental drawback of active metasurfaces is access to a limited phase modulation range $\Delta\varphi = \varphi_{max} - \varphi_{min}$. In addition, for the active metasurface discussed here, Fig. 2.2 illustrates that a maximal phase shift of 272° is achieved with a bias application of ±6 V. Since these levels approach values that are marginal to the breakdown field in the active ITO layer, it is desirable to operate at lower voltage and therefore a lower phase modulation range to increase device lifetime. Thus, for the purpose of this study, we limit the applied bias range to ±4.5 V in the modeled active metasurface [42]. For further reduction in $\Delta\varphi$, the phase modulation is truncated symmetrically around the ENZ permittivity transition at 2.75 V. This simultaneously also ensures minimal amplitude modulation A_{mod}, which is desirable for enhanced performance.

Figure 2.5 illustrates the effect of a reduced $\Delta\varphi$ of the field-effect tunable metasurface on the performance of forward- and inverse-designed arrays steering at $\theta_r = 18.3°$. The underlying design principle of forward-designed arrays with stairstep phase profiles does not account for the covariation of phase with amplitude. Thus, decreased phase modulation ranges lead to significant power coupling into undesired sidelobes, as illustrated in the right column of Fig. 2.5 (gray). In contrast, inverse design facilitates highly directive beams even with a limited phase modulation range of 210° where directivity is enhanced by up to 55% compared to the respective stairstep forward design (Fig. 2.5d). As the phase modulation range is reduced further, a decrease in the optimized directivity is observed, with increasing sidelobe amplitude at 0° and $-\theta_r$ (Fig. 2.5f, h). Nonetheless, the optimized directivity re-

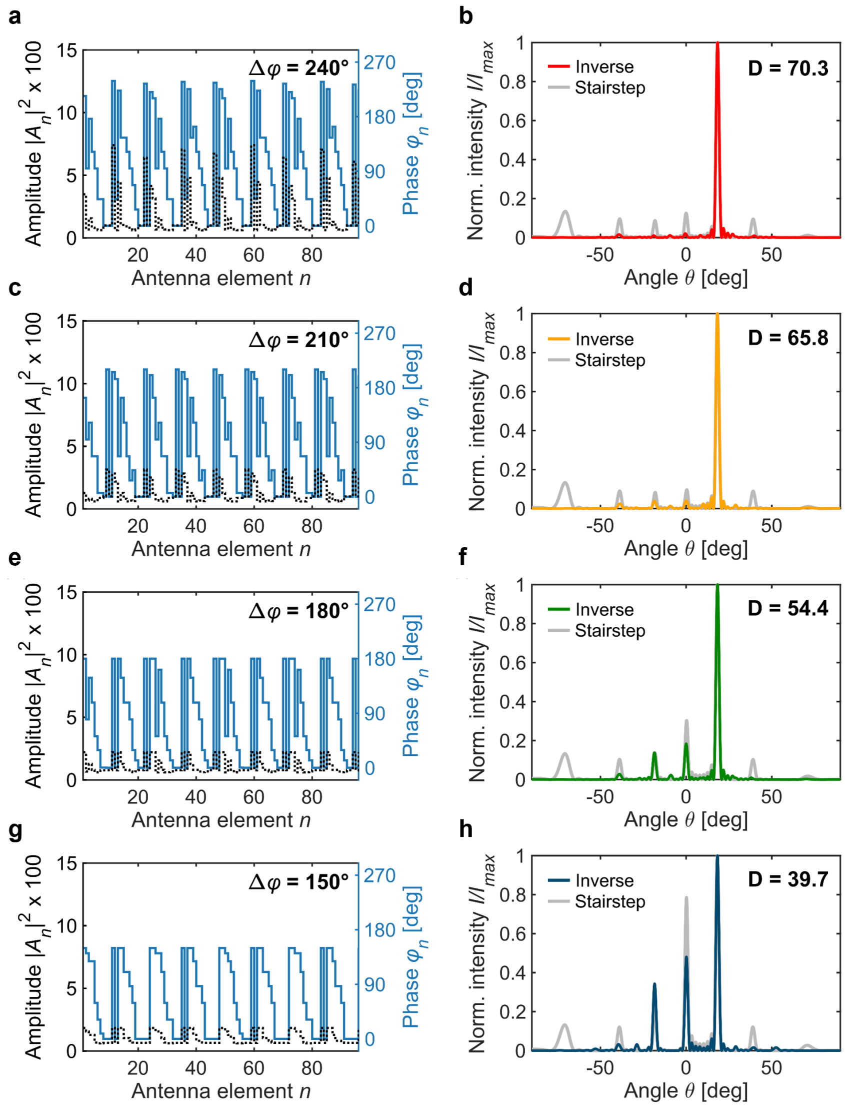

Figure 2.5: **Optimized beam steering with reduced phase modulation.** Optimized phase and amplitude designs for steering at $\theta_r = 18.3°$ with reduced phase modulation ranges $\Delta\varphi$ of (a) 240°, (c) 210°, (e) 180°, and (g) 150° for the active metasurface shown in Fig. 2.2. Panels (b), (d), (f), and (h) illustrate the normalized far-field intensity $I/I_{\max}$ as function of polar angle θ for the inverse-designed array phase and amplitude profiles as well as the forward-designed stairstep phase profile (gray). The optimized directivity with reduced $\Delta\varphi$ is labeled in the upper right corner of the figure.

ported with $\Delta\varphi = 150°$ (Fig. 2.5h) is 41% higher than the corresponding forward design and comparable to the directivity of the stairstep phase profile introduced with $\Delta\varphi = 270°$ in Fig. 2.5d.

The results discussed here underscore the ability of array-level inverse design to create high-performing arrays despite covarying phase and amplitude. However, they do not allow for any decoupled conclusions on the independent effects of phase and amplitude modulation on the optimized performance. Hence, we studied a series of hypothetical metasurfaces with limited phase modulation, where amplitude was held at a constant value $A = 1$. In addition, we artificially generated representative trial values of the amplitude-voltage relation with modest amplitude modulation where the phase modulation range was held at a constant value of $\Delta\varphi = 360°$. For generality, the arrays considered here consist of 100 antennas spaced at a period of 400 nm, with an operating wavelength of 1550 nm.

Figure 2.6a demonstrates the optimized directivities for active metasurfaces with constant, unit amplitude and varying phase modulation range $\Delta\varphi$. Phase is assumed to be a sigmoidal function of the applied bias. As $\Delta\varphi$ is reduced, directivity is maintained up to a threshold phase modulation range $\Delta\varphi_{\text{threshold}}$. With further distortion in the information carried by each element, destructive interference results in intensified sidelobes that reduce directivity. We define $\Delta\varphi_{\text{threshold}}$ as the phase modulation range required to obtain the threshold directivity of $0.9 \times D_{\text{ideal}}(\theta_r)$, where $D_{\text{ideal}}(\theta_r)$ corresponds to the directivity of an ideal, forward-designed antenna array. Figure 2.6b compares $\Delta\varphi_{\text{threshold}}$ for forward-designed antenna arrays with linear truncated phase profiles to those of the corresponding inverse designs. Our results indicate that inverse design lowers the required phase modulation range to obtain threshold performance by a considerable amount. By introducing disorder into the phase profile, inverse design succeeds in suppressing power coupled into undesired directions. Thus, the inverse design approach outperforms intuitively motivated forward design for reduced phase modulation range. The difference in $\Delta\varphi_{\text{threshold}}$ becomes particularly noticeable at large steering angles due to an additional reduction of the FWHM, as discussed in Fig. 2.4d.

In contrast, we consider antenna arrays exhibiting a phase modulation range of 360° but nonideal amplitude characteristics, as shown in Fig. 2.6c. The three different amplitude profiles represent distinct cases: constant amplitudes, linear functions, and Lorentzian line shapes. To obtain comparable results, the amplitude modulation of the two latter cases is chosen to be $A_{\text{mod}} = 20.0$. Figure 2.6d shows a comparison

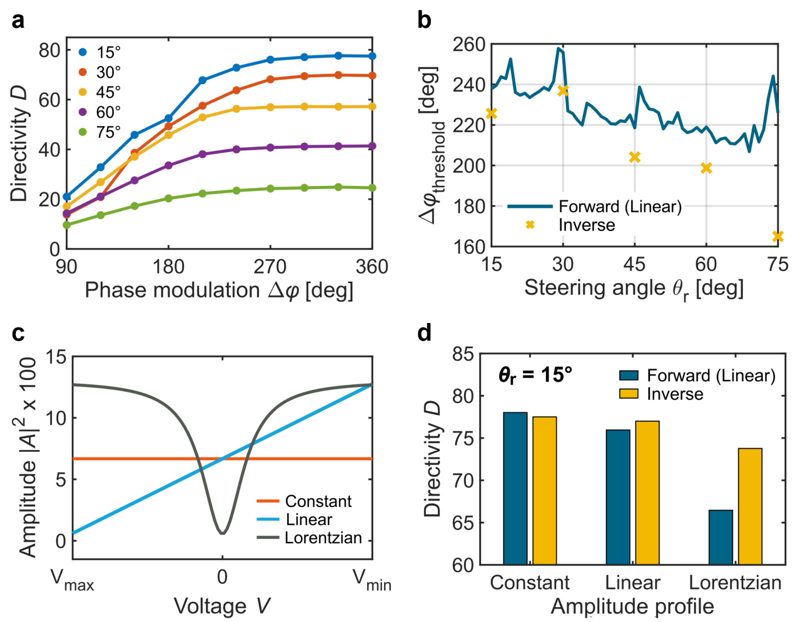

Figure 2.6: **Impact of phase and amplitude modulation on beam steering performance.** Analysis of a series of hypothetical structures consisting of a 1D array of 100 antennas uniformly spaced at 400 nm. The operating wavelength is λ = 1550 nm. (a) Optimized directivity D *vs* phase modulation range $\Delta\varphi$ for a metasurface with constant amplitude $A = 1$. Optimized results are shown for steering at $\theta_r = 15°$ (blue), 30° (orange), 45° (yellow), 60° (violet), 75° (green). (b) Required phase modulation $\Delta\varphi_{threshold}$ for threshold directivity of $0.9 \times D_{ideal}(\theta_r)$ *vs* steering angle θ_r for forward (blue) and inverse designs (yellow). (c) Trial amplitude A as a function of bias voltage V for three distinct cases: constant (orange), linear (blue), Lorentzian (gray). V_{min} and V_{max} are the minimal and maximal applied voltages, respectively. (d) Directivity D of forward-designed, linear phase profiles and inverse-designed arrays using amplitude relations shown in (c). The phase modulation corresponds to $\Delta\varphi = 360°$ and the steering angle is $\theta_r = 15°$.

of the directivity values obtained with forward and inverse designs for steering at $\theta_r = 15°$. For constant amplitude, the directivity of both forward- and inverse-designed arrays is ideal. Minor variations in the optimized directivity are attributed to the stochastic nature of the algorithm. In comparison, linearly varying amplitude leads to lower directivities. However, due to the assumed sigmoidal variation of phase across the applied bias, amplitudes vary minimally over a large segment of the phase modulation range. As a result, near-ideal performance can be attained with both forward and inverse design. In the case of the Lorentzian amplitude profile, however, the largest change in phase occurs precisely in the low amplitude regime. This introduces a considerable difference in the performance of forward and inverse designs. An analysis of the optimized amplitude profile (Fig. 2.7a) indicates that even though there is no significant difference in A_{mod}, inverse design can suppress undesired sidelobes, as shown in Fig. 2.7b. This can be attributed to a change in the distribution of phases across 360° in both designs. Since forward designs are based on constant phase shifts between adjacent antennas, the distribution of phases over the entire array is nearly uniform (Fig. 2.7c). As a consequence, forward designs are highly sensitive to the antenna-specific amplitude profile and the directivity is reduced to $D_{\mathrm{Lorentz,forward}} = 0.85 \times D_{\mathrm{const,forward}}$. Inverse design, on the other hand, aims to avoid low amplitude regimes. Due to the sigmoidal phase modulation, minimal amplitude is reported for an acquired phase of 180°. Therefore, our optimization approach results in a considerably smaller number of antennas with acquired phase in that regime (Fig. 2.7d), resulting in higher directivitiy with $D_{\mathrm{Lorentz,inverse}} = 0.94 \times D_{\mathrm{const,forward}}$.

This study illustrates that array-scale inverse design is most beneficial for highly nonideal active metasurfaces that exhibit low amplitude under conditions of large phase shift. It is to be noted that such cases are typically reported in tunable structures that rely on intrinsic resonances. The results generated using array-level inverse design approach the ideal performance obtained for constant amplitude and a given phase modulation.

2.5 Experimental demonstration of array-level inverse design

Here, we experimentally validate the array-level inverse design approach for an active beam steering metasurface. The previously introduced metasurface was redesigned to ensure an operating wavelength of the fabricated metasurface around 1550 nm. Figure 2.8 shows the full-wave simulation results obtained using finite difference time domain (Lumerical FDTD) for a metasurface with the following layer thicknesses: t_{b} = 80 nm, t_{alumina} = 9.5 nm, t_{ITO} = 5 nm, t_{h} = 9.5 nm, and t_{a} = 40 nm. The antenna and electrode dimensions are defined as l_{a} = 210 nm, w_{a} = 160 nm, and w_{e} = 130 nm, respectively, and the period is d_x = 400 nm. Additionally, we added a 60 nm thick silica (SiO_2, t_{c}) capping layer to increase device durability (Fig. 2.9a). A scanning electron microscopy (SEM) image of the metasurface is shown in Fig. 2.9b. We would like to note that the period of the metasurface post-fabrication was measured to be d_x = 430 nm.

Once the metasurface was fabricated (as outlined in Section A.2 of the Appendix), we measured the spectra of the reflected light intensity (*i.e.*, reflectance) and phase in

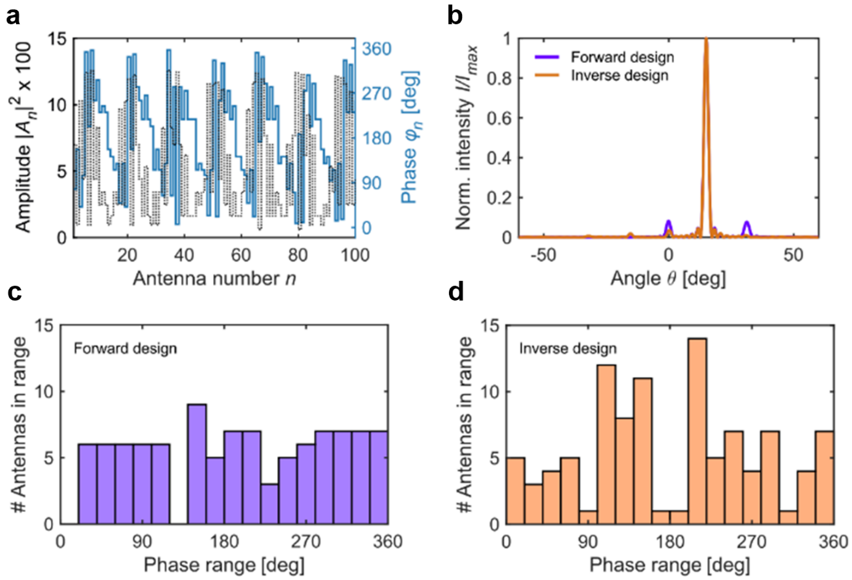

Figure 2.7: **Array-level inverse design of amplitude-modulated array with Lorentzian modulation.** (a) Optimized phase and amplitude profile over 100 antennas. The Lorentzian amplitude modulation shown in Fig. 2.6 is associated with a 360° sigmoidal phase modulation. (b) Normalized far-field intensity $I/I_{\max}$ as function of polar angle θ for forward (linear truncated, violet) and inverse-designed (orange) arrays. The distribution of number of antennas in various phase ranges of 20° between 0° and 360° is displayed in (c) for forward design and (d) for inverse-designed array profiles.

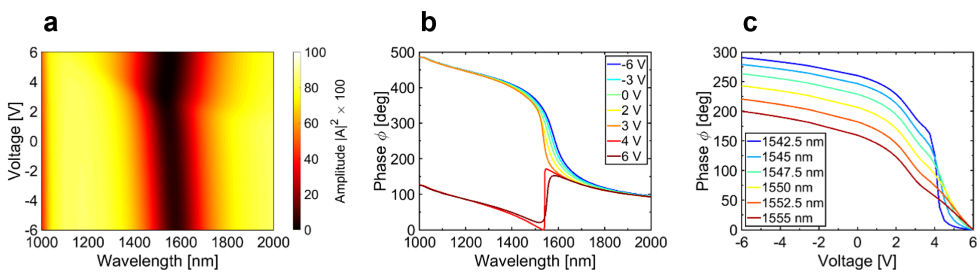

Figure 2.8: **Full wave simulations of experimentally realized metasurface.** (a) Reflectance as function of wavelength and applied bias voltage. (b) Acquired phase spectrum at different applied biases. (c) Acquired phase as function of applied bias at different wavelengths.

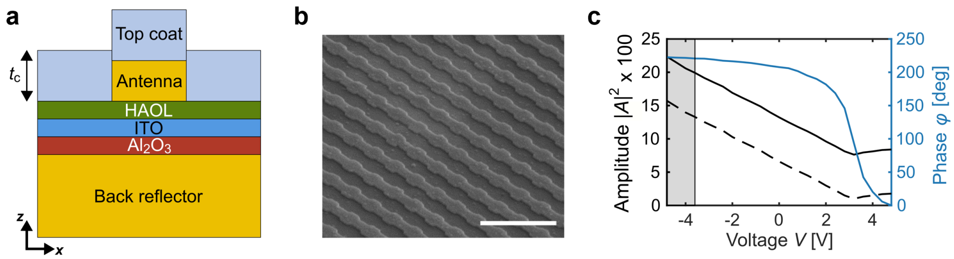

Figure 2.9: **Experimentally realized metasurface and gate-tunable optical response.** (a) Side-view schematic of the experimentally fabricated metasurface with a SiO_2 top-coat layer with thickness t_c. (b) SEM image of the fabricated nanoantennas with a scale bar of 1 μm. (c) Measured phase shift (blue) and reflectance (black) as function of the applied bias voltage. The dashed black line indicates the approximated reflectance contributing to the beam steering performance. Phase/amplitude values within the gray box were not used for optimization.

order to characterize the tunable optical response of the metasurface under different applied biases. To do so, we measured the amplitude and phase of the reflected light using a tunable NIR laser in the wavelength range of 1420 nm – 1575 nm. The phase shift of the reflected light was determined using a Michelson interferometer in which interference fringe patterns were generated by the superposition of the beam reflected from the metasurface and the incident reference beam. The acquired phase shift was then extracted by fitting the interference fringe patterns to sinusoidal functions. The experimental setup and the procedure for phase and reflectance measurements is described in Section A.3 of the Appendix. The voltage-tunable optical response of the metasurface was then characterized by measuring the amplitude and phase of the reflection from the nanoantenna array while changing a bias voltage that was collectively applied to all antennas, resulting in a uniform change in phase across the metasurface.

Figure 2.9c shows the experimentally measured reflectance as well as a total acquired phase shift of 223° for the light reflected from the fabricated metasurface. The operating wavelength was chosen to be λ = 1548 nm such that the phase shift provided by the metasurface could be maximized. Notably, considerably larger amplitudes than those reported in full-wave simulations are obtained. This phenomenon has been observed previously [42, 53] and is attributed to a misalignment in the incident polarization. As the misaligned component of the incident light does not interact with the antenna, this effect leads to increased reflected intensity normal to the metasurface. Furthermore, since the misaligned component does not contribute to the accumulated phase shift, we assume reduced reflectance to approximate the actual amplitude contributing to the beam steering performance. Thus, a constant offset of $\Delta_r = 6.6\%$ is subtracted from the measured reflected light intensity (dashed line in Fig. 2.9c), leading to a minimum reflectance of 1%. The offset was accounted for in the array factor calculation by increasing the intensity at $\theta = 0°$ by $\Delta_r = 6.6\%$. This approach was verified for previously measured far-field radiation patterns obtained using forward design [42], as discussed in Section A.4 of the Appendix. Finally, array-level optimization was performed using the measured phase shift and the actual approximated amplitude. Due to the difference between the work functions of Au and ITO, the ITO layer is slightly depleted at zero applied bias [30]. Thus, to avoid breakdown of the gate dielectric during beam steering measurements, we omit bias voltages below -3.6 V. Hence, a bias voltage range of [-3.6 V, +4.8 V] was used for the optimization, as indicated by the gray box in Fig. 2.9c. As a result, a phase shift of $\Delta\phi = 221°$ was obtained.

The forward-designed and optimized array phase and amplitude profiles for experimental demonstration are shown in Fig. 2.10a and b, respectively. We confirmed through full-wave simulations of the forward- and inverse-designed array profiles that the fabricated reflectarray metasurface could be treated using the independent scatterer approximation, as shown in Fig. 2.11, vindicating our approach to an array-level inverse design.

Figure 2.12a illustrates the analytically obtained beam steering performances using forward-designed four-level stairstep phase profiles with repetition numbers (RN) varying from RN = 3 to 6 (Fig. 2.10a). The far-field radiation patterns for forward design are illustrated in gray, and the corresponding results obtained using array-level inverse design are overlaid in color. As can be seen, even though sidelobes are not entirely removed due to a reduced phase modulation with covarying amplitudes, a considerable sidelobe suppression that increases beam directivity is achieved (Table 2.1). We note that while the optimization was performed for the entire half-space (*i.e.*, additional sidelobes at larger polar angles were suppressed to increase directivity), we only visualize and evaluate the directivity for the experimentally detectable range from $-23°$ to $+23°$.

As a comparison, the experimental measurements for the beam steering active metasurface using forward- and inverse-designed array profiles are illustrated in Fig. 2.12b. Increased sidelobes as well as increased relative intensities compared to the analytically computed case, in particular for the specularly reflected light, are

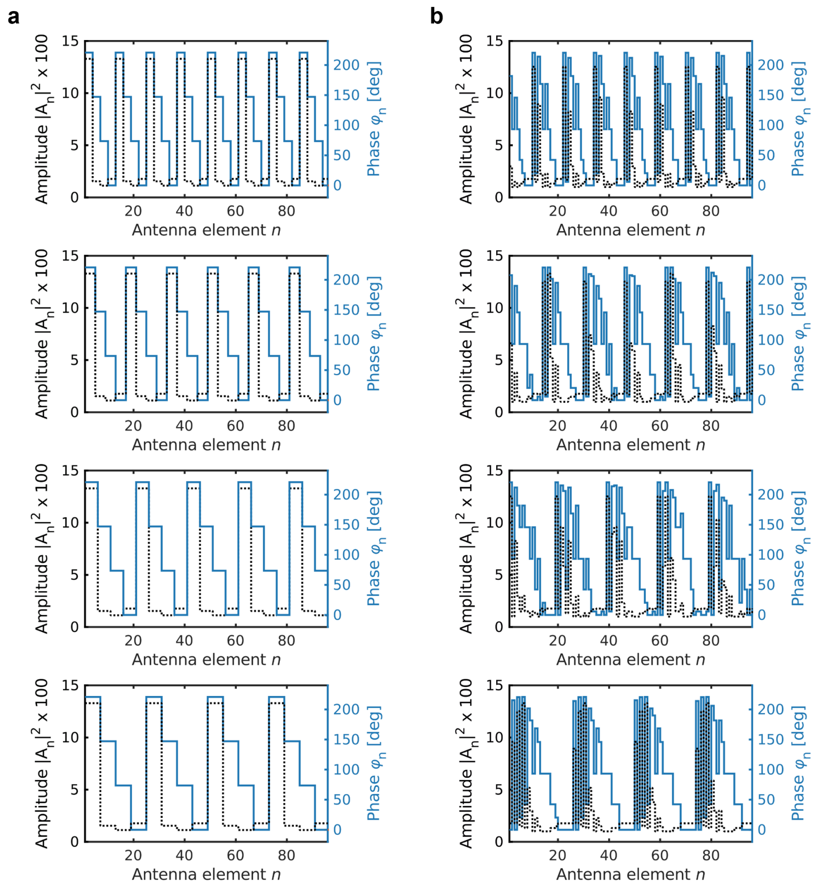

Figure 2.10: **Forward-designed and optimized array profiles for experimental demonstration.** Spatial array amplitude (black) and phase (blue) profiles for (a) forward and (b) inverse design used in experiments. In (a), the repetition number of the stairstep phase profile is varied from RN = 3 (top) to 6 (bottom).

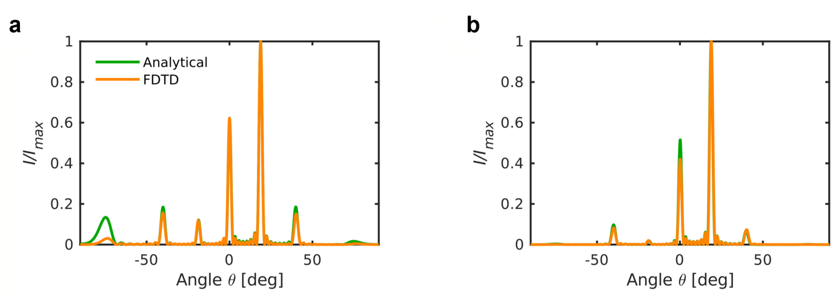

Figure 2.11: **Comparison of far-field radiation patterns with array-factor calculations (green) and FDTD simulations (orange).** Normalized intensity $I/I_{\max}$ *vs* polar angle θ with (a) stairstep forward design with a repetition number of RN =3, and (b) array-level inverse design approach. The operating wavelength is λ = 1545 nm.

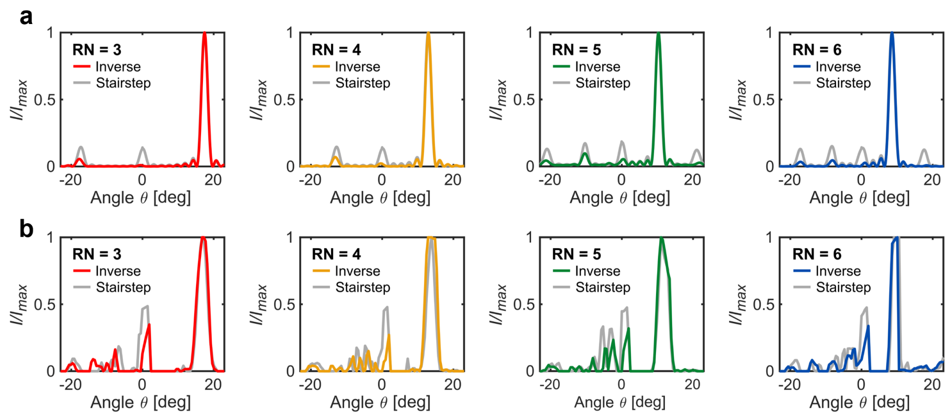

Figure 2.12: **Experimental demonstration of beam steering with forward and array-level inverse design.** (a) Analytically calculated and (b) experimentally measured far-field radiation patterns obtained using forward- (gray) and inverse-designed array profiles (colored). Forward designs are obtained using a four-level stairstep phase profile with repetition number varying from RN = 3 to 6 (left to right). All figures are plotted for the experimentally detectable angular range from $-23°$ to $+23°$.

	analytical, forward	analytical, inverse	experimental, forward	experimental, inverse
$\theta_r = 17.4°$ (RN = 3)	16.1	19.8 (+23%)	8.7	9.7 (+11%)
$\theta_r = 12.9°$ (RN = 4)	16.2	19.6 (+21%)	10.2	9.8 (-5%)
$\theta_r = 10.3°$ (RN = 5)	13.9	18.3 (+32%)	8.4	9.6 (+15%)
$\theta_r = 8.5°$ (RN = 6)	13.8	19.7 (+43%)	9.6	12.0 (+25%)

Table 2.1: **Analytically computed *vs* experimentally measured directivity *D* for** $\theta = [-23°, +23°]$.

reported in both forward and inverse design. Notably, in the experiments conducted for stairstep phase gradient profiles with repetition numbers varying from 3 to 6 (*i.e.*, RN = 3, ..., 6), inverse design has resulted in an overall reduction in reflected optical power that is spuriously radiated outside the main steered beam, including specularly reflected power. The discrepancies in the amount of power radiated into undesired sidelobes between the analytical computations and experimental measurements are caused by the interplay of several effects, including antenna reflectances that are different from the assumed values, as well as a reduction in the available phase modulation range. Reduction in the achievable phase modulation range is caused by extrinsic damage from application of large bias voltages which results in a change in the leakage current as well as the breakdown field of the gate dielectric. Figure 2.13 shows the phase reduction over three consecutive measurements for two different metasurfaces to illustrate this effect. Since the fabricated metasurface operates around phase modulation values that are near the previously reported values of $\Delta\varphi_{\text{threshold}}$ (Fig. 2.6b), further reduction in the phase modulation range can result in deviations of the beam steering performance from that analytically predicted using both forward- and inverse-designed array profiles. Furthermore, it should be noted that small variations in nanoantenna size can be introduced during metasurface fabrication. As a result, one can expect inconsistencies in amplitude and phase for individual scattering elements compared to the collectively measured optical response. Since the current experimental capabilities do not allow for an amplitude and phase measurement on a single-antenna basis, the notion of a phase/amplitude error becomes a crucial topic of discussion that is further investigated in the subsequent section. Notwithstanding the mentioned challenges, we were able to demonstrate that nonintuitive, inverse-designed array profiles can reduce spurious power coupled into sidelobes and thus enhance beam steering performance. For the measurements shown in Fig. 2.12b, a maximal increase in directivity of 25% was obtained in comparison to the respective forward design for $\theta_{\text{r}} = 8.5°$ (Table 2.1). In addition, inverse design decreased specular reflection by an average of 33%. We note that a broadening of the main lobe due to experimental angular resolution errors resulted in lower beam directivity for $\theta_{\text{r}} = 12.9°$ (RN = 4). Nonetheless, the peak sidelobe intensity was reduced by 43% in this case.

2.6 Beam steering arrays with phase disorder

The experimental realization of optimized, nonintuitive array designs is challenged by various sources of nonideality, error and noise, such as discrepancies in actual phase and amplitude as a result of inconsistent nanoantenna sizes post-fabrication, errors in bias application or interantenna coupling. The validity of the independent scatter model was verified *via* full wave electromagnetic simulation for both forward and inverse design in the case of the experimentally studied transparent conducting oxide metasurface (Fig. 2.11). However, this fundamental assumption becomes nontrivial for alternative metasurface platforms exhibiting leaky resonant modes. As a consequence, the resulting deviation from the optimized phase and amplitude

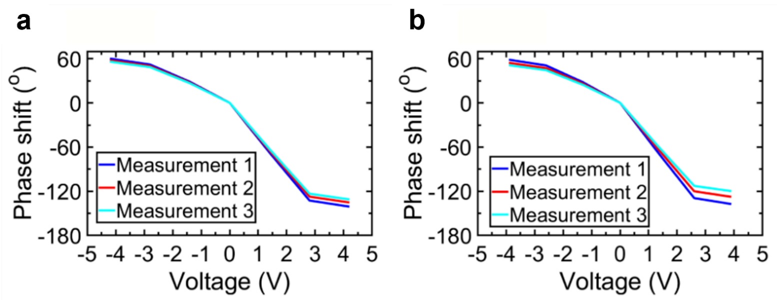

Figure 2.13: **Reduction in phase shift over consecutive measurements.** (a) A maximum phase shift of 201°, 193°, and 187° was obtained for the first test sample in the first, second, and third round of the phase measurement, respectively. (b) The phase modulation provided by the second test sample was measured to be 196°, 182°, and 171° in three consecutive measurements.

profiles are expected to cause additional scattering in undesired directions that lowers the directivity.

Here, we perform a sensitivity analysis of the optimized designs to error and noise. To do this, we systematically introduce random phase noise and identify threshold values beyond which a strong decrease in directivity is observed. We characterize f as the fraction of antennas in the array differing from their original phase value $\varphi_{\text{original}}$. The phase disorder range δ further quantifies the maximal amount of phase error at each deviating element (Fig. 2.14a). The disordered phase values $\varphi_{\text{disorder}}$ are calculated as

$$\varphi_{\text{disorder}} = \varphi_{\text{original}} + \text{rand}\left[-\frac{\delta}{2}, +\frac{\delta}{2}\right]. \tag{2.9}$$

Here, rand$[x, y]$ computes a uniformly distributed random value between x and y. Capping of $\varphi_{\text{disorder}}$ at the minimal and maximal phase values ensures that upon adding phase noise, the antenna phase stays within the available phase modulation range. To account for the covarying amplitude and phase, $\varphi_{\text{disorder}}$ is additionally mapped to the corresponding amplitude, which is obtained from the antenna-specific optical response.

Figure 2.14b illustrates the error tolerance of an inverse-designed array phase profile for our example field-effect tunable active metasurface steering at $\theta_r = 18.3°$ (Fig. 2.4a). The optimized array design is insensitive to small phase errors corresponding to small f and/or small δ. In the limiting case of $f = 100\%$, phase error is introduced

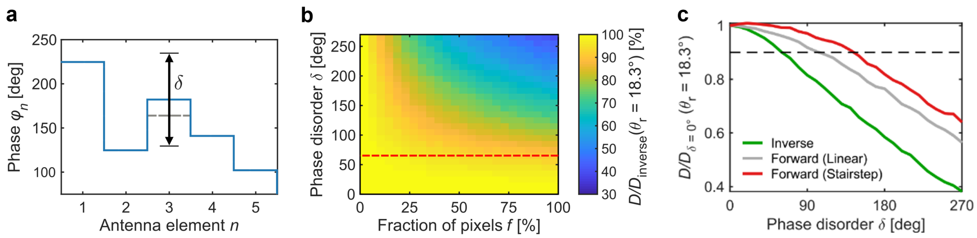

Figure 2.14: **Phase noise introduction in spatial phase profile.** The phase disorder range δ is defined such that it allows distortion of each antenna phase by a uniformly distributed random phase value between 0° and $\pm\delta/2$. The schematic illustrates a phase disorder range of $\delta = 100°$. The gray dashed line represents the disordered phase value. (b) Phase disorder range δ *vs* fraction of antennas f that are changed from their original value for the optimized array design illustrated in Fig. 2.4a for $\theta_r = 18.3°$. The red dashed line marks the threshold performance of $0.9 \times D_{\mathrm{inverse}}$ in the limiting case of $f = 100\%$. (c) Relative change in directivity for increasing phase disorder δ for steering at $\theta_r = 18.3°$ for inverse-designed arrays (green), forward-designed linear (gray) and stairstep (red) phase profiles. The black dashed line marks the threshold directivity. The data sets in (b) and (c) are averaged over 100 implementations.

into every antenna in the entire array. This case is characteristic of interantenna coupling that would lead to a distortion of the phase at each antenna due to its nearest neighbors. Our analysis shows that optimized designs can tolerate up to ±30° phase error ($\delta = 60°$) before reaching the directivity threshold of $0.9 \times D_{\mathrm{inverse}}$. In comparison, our analysis shows that the threshold performance of $0.9 \times D_{\delta=0°}$ is obtained for larger amounts of phase disorder δ in the case of forward designs. As shown in Fig. 2.14c, $\delta_{\mathrm{inverse}} = 60° < \delta_{\mathrm{forward,lin}} = 100° < \delta_{\mathrm{forward,step}} = 140°$. Here, $D_{\delta=0°}$ is the beam directivity of the respective array design without any introduction of phase noise. It is to be noted that directivities of stairstep profiles can surpass $D_{\delta=0°}$ for $\delta \leq 40°$. Since stairstep designs represent simplified gradient phase profiles, small amounts of phase disorder can lead to closer resemblances to higher-directivity linear array designs. The reduced error tolerance for inverse design is understandable, considering that the nonintuitive inverse-designed arrays typically exhibit more disordered phase profiles, even prior to any introduction of noise. As a result, they tolerate smaller errors before reaching substantial loss of information. Nonetheless, the findings reported in this analysis imply a considerable tolerance of phase noise for inverse-designed spatial array profiles.

2.7 Realizing advanced metasurface functionalities

Until now, our focus was on using array-level optimization for the demonstration of optimized beam directivity. Based on the target application, however, it might be desirable to realize alternative metasurface functions. In the following, we apply the iterative optimization approach introduced in Section 2.3 to optimize the spatial phase and amplitude configuration for (i) maximal power efficiency of the steered beam given a nonideal antenna response, (ii) the creation of flat top beams and beams with variable widths, and lastly (iii) simultaneous steering of beams in two desired directions.

Power efficiency of steered beams

The FOM quantifying the beam steering performance in this work was chosen to be the beam directivity D. It is a unitless quantity that depends on the ration of the intensity at the desired steering angle θ_{r} to the amount of power scattered into all directions normalized by the solid angle, as discussed in Eq. (2.4). Thus, it remains unaffected by scaling of the far-field radiation patterns by a constant (intensity) factor. Directivity is a common metric used to analyze the performance of RF phased arrays. An ideal metasurface array with $d_x = 400$ nm operating at $\lambda = 1550$ nm ($d_x/\lambda \sim 0.25$) approaches performances that are reported with an array of parallel short dipoles [72]. In addition, the optimized sidelobe level reported in this work corresponds to values that are generally obtained for phased arrays with a complete phase modulation over 360° [73].

The power efficiency η is determined by the absolute amount of power that is steered into the main lobe compared to the total input power. For an array profile with varying amplitudes, η is calculated as

$$\eta(\theta_{\mathrm{r}}) = \frac{P_{\mathrm{m}}(\theta_{\mathrm{r}})}{P_{\mathrm{scat}}} \cdot A_{\mathrm{eq}} \tag{2.10}$$

where P_{m} is the power scattered into the main lobe steering at θ_{r} and P_{scat} is the total scattered power. The ratio of P_{m} and P_{scat} is multiplied by the equivalent amplitude A_{eq} that would be required in an array of antennas with constant amplitude to generate an equivalent amount of scattered power. Thus, $A_{\mathrm{eq}} = P_{\mathrm{scat}}/P_{\mathrm{input}}$ with P_{input} being the input power. Note that P_{input} can be determined by assuming an ideal reflectarray with constant, unit amplitude and a complete phase modulation over 360°.

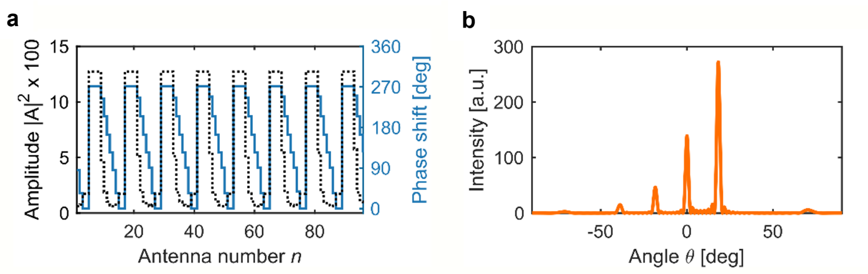

Figure 2.15: **Optimization for power efficiency.** (a) Inverse-designed array amplitude (black dotted) and phase (blue) profiles and (b) far-field radiation patterns for a power efficiency optimization. The optimization was performed based on the optical response of the field-effect tunable metasurface introduced in Fig. 2.2.

Due to the strong absorption in the active antenna element [42, 74], the power efficiency of the beam steering arrays studied in this work is strongly limited. Consequently, the optimized directivity discussed in Section 2.3 (Fig. 2.4a, b) results in a power efficiency of 0.9%, even though 86% of the total scattered power is directed into the main lobe. Here, we demonstrate as a proof-of-concept that the same inverse design algorithm can also be applied to a power efficiency optimization. For this purpose, the figure of merit is adapted to FOM = $\eta(\theta_r)$. Figure 2.15a shows the optimized array profile as well as the corresponding radiation pattern (Fig. 2.15b) for optimal power efficiency at $\theta_r = 18.3°$. It is to be noted that the increase in power efficiency comes at the cost of beam directivity, as the algorithm aims to increase the occurrence of large amplitudes in the antenna array to enhance efficiency. Therefore, the amplitude modulation increases, leading to a reduction in beam directivity. Meanwhile, the opposite trend holds true for a directivity optimization: Inverse design aims to minimize amplitude modulation to reduce sidelobes. As the main phase shift occurs in a low amplitude regime, the minimization of amplitude modulation results in reduced power efficiencies. For reference, the corresponding directivity and efficiency values are tabulated in Table 2.2.

	Directivity D	Efficiency η
Forward design, stairstep	39.5	2.1%
Inverse design, directivity opt.	72.7	0.9%
Inverse design, efficiency opt.	41.9	2.7%

Table 2.2: **Optimized directivity D and efficiency η for steering at θ_r** = 18.3°.

As the scattered light amplitudes are the limiting factor for power efficiencies in beam steering metasurfaces, we would like to remark that they can be strongly enhanced with the use of active metasurfaces exhibiting higher reflectance or transmittance values, such as all-dielectric metasurfaces [20, 35, 75].

Variable beam widths and flat top beams

The beam width (or FWHM) is determined by the aperture size and varies as function of steering angle, as illustrated in Fig. 2.4. Based on the specific modality of optical imaging or sensing, it may be beneficial to control the beam width in addition to the steering angle to ensure uniform information collection from all directions. While the minimal beam width of light scattered from an array of antennas is fixed by the aperture size, we can use array-level inverse design to generate spatial phase and amplitude configurations that result in larger beam widths. This can be used in cases where, *e.g.*, coarse sampling of a scene is desired before finer details are imaged [76]. In the following, we illustrate first the generation of variable beam widths for a steered beam with an ideal metasurface and then demonstrate realization of flat top beams using the nonideal active metasurface introduced in Fig. 2.2.

Figure 2.16 shows the forward-designed and optimized spatial phase profiles for an ideal metasurface with 360° phase modulation and unity amplitude steering a beam at $\theta_\mathrm{r} = 20°$. Similar to the case studied in Fig. 2.1, we assume an aperture with 100 antennas arranged at a spacing of $d_x = 400$ nm operating at 1550 nm. Given the metasurface aperture, conventional forward design of the phase profile yields a beam with a FWHM of 2° (Fig. 2.1a, b). To design array profiles yielding a target FWHM, F_t, we write our objective function as a minimization problem with

$$\mathrm{FOM}(F_t, \theta_\mathrm{r}) = 50 \cdot |\mathrm{FWHM}(\theta_\mathrm{r}) - F_t| + 10 \cdot \frac{I_{\mathrm{max},2}}{I(\theta_\mathrm{r})} + \frac{\mathrm{avg}\Big(I\big(\theta_\mathrm{r} - \frac{F_t}{2}\big), I\big(\theta_\mathrm{r} + \frac{F_t}{2}\big)\Big)}{\int I(\theta)\mathrm{d}\theta}. \tag{2.11}$$

Here, the first term aims to minimize the difference between the FWHM of the beam steered at θ_r and the target FWHM, F_t, the second term aims to maximize the peak intensity at the target angle θ_r in comparison to the second largest peak, and the last term is an adapted directivity term which aims to maximize intensity across the FWHM while minimizing undesired sidelobes in all directions. The FOM is formulated as a weighted sum, where the weights are chosen such that they yield optimal radiation patterns for a range of target F_t values. The optimized spatial phase

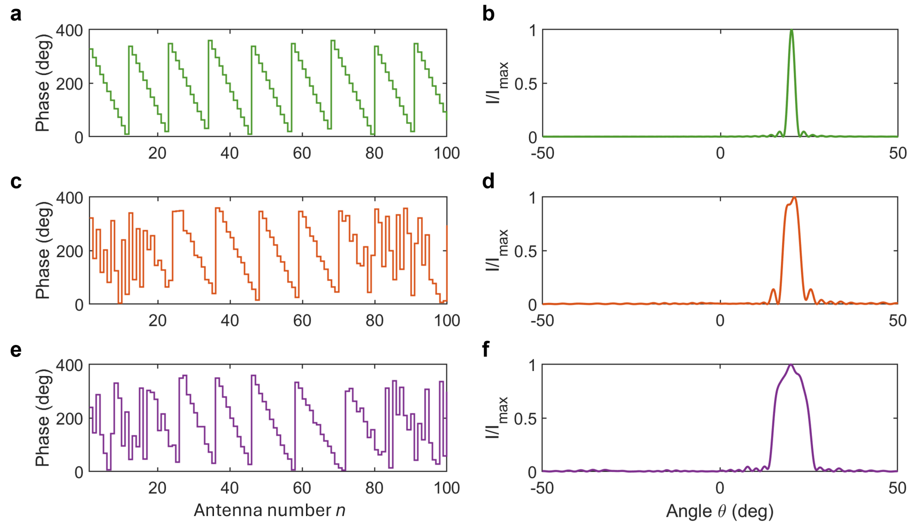

Figure 2.16: **Variable FWHM of steered beam with ideal metasurface.** Spatial phase profile over an array of 100 antennas spaced at d_x = 400 nm (left) and corresponding normalized intensity *vs* polar angle at λ = 1550 nm (right). The three cases illustrate forward design (green; a, b), optimization for a FWHM of 5° (orange; c, d), and optimization for a FWHM of 10° (violet; e, f). Ideal antenna properties, *i.e.*, unity amplitude and 360° phase modulation, are assumed for this optimization.

profiles and the corresponding radiation patterns for F_t = 5° (Fig. 2.16c, d) and F_t = 10° (Fig. 2.16e, f) are shown as exemplary cases. The optimization appears to artificially reduce the aperture of the metasurface by imposing a phase gradient over a smaller subset of antennas (‘steering aperture’) and setting noninutitive phase values outside (‘nonsteering aperture’). Similar approaches with forward design of the nonsteering aperture with constant phase values result in strong specular reflection. Therefore, further studies are needed to analyze the degree of phase randomness required in the nonsteering aperture to yield a tunable FWHM with low sidelobe levels. Nevertheless, for realistic active metasurface designs, the use of array-level inverse design is expected to yield improved results by additionally taking into account the device-specific optical response.

In applications that require a uniform illumination across a range of angles, the objective changes to generating flat top beams rather than having beams with a wider FWHM, as shown in the example above. For this, the FOM is chosen to be one that minimizes the difference of the actual radiation pattern from a target radiation pattern, where the target radiation pattern resembles an angular pass-band with zero and one normal intensity regimes. Figure 2.17 shows the optimized array

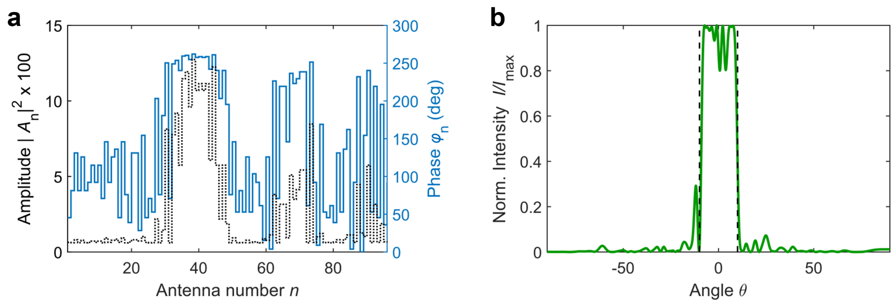

Figure 2.17: **Flat top beam with nonideal active metasurface.** (a) Inverse-designed array amplitude (black, dotted) and phase (blue) profiles and (b) corresponding normalized intensity as function of polar angle for nonideal active metasurface introduced in Fig. 2.3. The black dashed lines at ±10° indicate the target angular width of the flat top beam.

phase and amplitude profile as well as the corresponding radiation pattern for a flat top beam with an angular width of ±10°. In this case, the optimization is performed for the nonideal active metasurface introduced in Section 2.3. Despite the nonideal optical response, the optimization algorithm is able to generate nearly uniform intensity across the target angular range with minimal undesired sidelobes. The uniformity of illumination can potentially be further improved by implementing constraints that limit the deviation of the actual normalized intensity from unity; however, this is likely to come at the cost of increased sidelobes.

Simultaneous steering of multiple beams

Until now, the focus of the optimization was to control the properties of one steered beam. However, the same array-level optimization can also be used to generate nonintuitive spatial amplitude and phase profiles that can simultaneously steer multiple beams in independent directions. This function could be used for increased scanning speeds in optical sensing applications, or for simultaneous detection of multiple objects. Here, we illustrate this principle based on the example of two independently steered beams with the nonideal active metasurface introduced above. The FOM that needs to be minimized for this purpose is chosen to be

$$\mathrm{FOM}(\theta_{\mathrm{r},1}, \theta_{\mathrm{r},2}) = \frac{1}{I(\theta_{\mathrm{r},1})} + \frac{1}{I(\theta_{\mathrm{r},2})} + \int I(\theta)\mathrm{d}\theta. \tag{2.12}$$

Here, the first two terms aim to maximize the intensity at the target steering angles $\theta_{\mathrm{r},1}$ and $\theta_{\mathrm{r},2}$, and the last term aims to minimize sidelobes. In addition to this

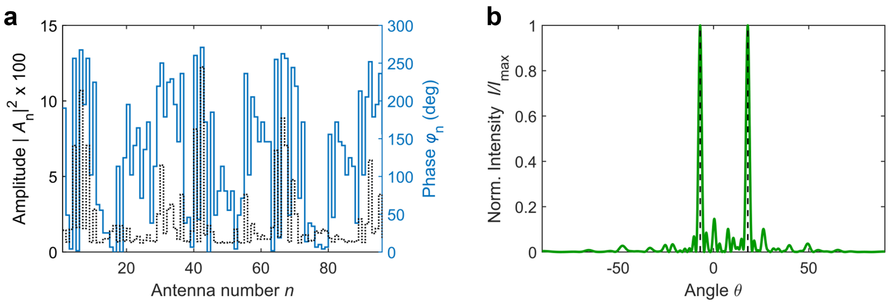

Figure 2.18: **Simultaneous steering of two beams at independent angles.** (a) Inverse-designed array amplitude (black, dotted) and phase (blue) profiles and (b) corresponding normalized intensity as function of polar angle for nonideal active metasurface introduced in Fig. 2.3. The black dashed lines indicate the target steering angles $\theta_{r,1} = -7°$ and $\theta_{r,2} = +18°$.

objective function, we implement constraints to fix the intensity of the two steered beams with respect to each other as well as the specularly reflected beam. For the results shown in Fig. 2.18 for two beams steered at $-7°$ and $+18°$, respectively, we also implemented two constraints requiring $I(\theta_{r,i}) \geq 8 \cdot I(\theta = 0°)$ with $i = 1, 2$ corresponding to the two beams. The steering angles were arbitrarily chosen in this example and similar results were observed for different sets of angles. It can be seen that while the optimization yields two directive beams steering at the target angles, there are an increased number of sidelobes compared to the case of a single steered beam. Due to this, we anticipate that scaling of this approach to an increased number of steered beams will require tolerance for larger sidelobe levels. In addition, continuous scanning of multiple independent beams with array-level optimization is a computation heavy problem. In Chapter 3, we will present an alternative, scalable approach for multi-beam steering using spatio-temporal modulation.

2.8 Outlook

Real-time array-level optimization

The array-level inverse design approach presented in this chapter is based on a numerical framework which assumes independent scatterers with localized modes. However, many recent designs utilize delocalized modes in nonlocal metasurfaces [77–79]. For such structures, we need to develop more sophisticated analytical models, or we must shift to performing array-level optimization using full-wave simulations instead [80]. This method, however, is considerably more computationally expensive and may restrict our abilities to compute the array configuration over a wide range of angles.

To address this challenge, one could perform real-time array-level optimization experimentally. For instance, in the case of beam steering metasurfaces, a camera could capture a Fourier space image at each iteration, which would then serve as an input for an optimization algorithm. The algorithm would extract the normalized intensity as a function of the polar angle and adjust the voltage configuration to optimize beam directivity. An iterative optimization similar to the one proposed in Section 2.3 could be adapted for this purpose. The primary source of time consumption would be image acquisition, rather than performing full-wave simulations for the entire array at each step. Ultimately, the computational time required would also depend on the number of antennas in the array that need to be configured to achieve a desired metasurface function. An additional benefit of this approach is that it could potentially account for experimental artifacts, such as nonuniform antenna widths, inhomogeneities in bias application, or slight misalignment, that may lead to spurious scattering in Fourier space.

Co-optimization framework for active metasurfaces

In many applications, it is necessary to not only optimize the directivity of steered beams but also maximize power efficiency. While the first part of Section 2.7 outlines a potential pathway for achieving this, power efficiency is ultimately constrained by the optical response of the antenna element, specifically, its scattered light amplitude and phase. In recent years, researchers have developed new design strategies to achieve higher efficiency active metasurfaces, including the use of various resonator designs yielding alternative electromagnetic modes [31, 80] and the exploration of new active materials [81–83].

Designing highly efficient active metasurfaces ultimately requires optimizing material choice, resonator design, and the overall system-level array design. In this context, the proposed array-level inverse design is crucial for the hierarchical co-design of both the array and the active antenna element in tunable metasurfaces. This approach aims to simultaneously optimize the array configuration *via* the external control variable, the nanoantenna shape, as well its complex dielectric function for a desired metasurface response. For practical implementation of hierarchical co-design, an incremental approach is most suitable. This would begin by combining array-level optimization with resonator design [84] and subsequently integrating resonator design with material choice, before developing a comprehensive optimization framework that addresses all three components simultaneously. Different optimization algorithms may be more suitable for different tasks. For example, resonator design (with a fixed material choice) could employ adjoint optimization [85–87] or machine learning [60, 88]. For optimizing and discovering new active materials, various data-driven strategies — such as machine learning, Bayesian optimization, density functional theory, and combinations thereof — could be pursued [89–92].

Enhancing control through space-time modulation

The final part of Section 2.7 proposes the use of array-level optimization for simultaneously controlling multiple independently steered beams. This approach enables control over both the angles and the relative intensities of the steered beams. While feasible for two beams, the optimization of the FOM becomes increasingly challenging as the number of beams increases, due to nonideal device characteristics.The complexity is further heightened when the beams are required to perform different dynamically tunable functions, such as steering and focusing.

In Chapter 3, we present a scalable approach for what we term *active mutlitasking* metasurfaces, which leverage space-time modulation [93–96]. In addition to the spatial modulation previously discussed, this approach utilizes high-frequency temporal modulation as an additional control variable. Temporal modulation of the metasurface at kHz to MHz frequencies allows for controlled frequency shifts in the scattered beam. By precisely tailoring the waveform applied to each metasurface electrode, we demonstrate the ability to independently control the spatial properties of beams with different frequency shifts. This method offers a scalable solution for controlling a large number of independent beams, theoretically limited only by the bandwidth of the experimental setup. We will discuss practical limitations and trade-offs between multiplexing and power efficiency in detail in the following chapter.

2.9 Conclusions

In conclusion, we have developed a versatile array-scale inverse design approach for active metasurface antenna arrays. Inverse design allows the array phase and amplitude profiles to be prescribed by change in the operating parameters of identical active antennas, rather than by geometrical shape optimization of individual antennas. We found that iterative optimization gives rise to nonintuitive array designs that enable high-directivity beam steering with nonideal antenna components.

Specifically, for the field-effect tunable metasurface analyzed here, directivities were enhanced by up to 84% compared to previously demonstrated forward designs, with sidelobe suppression approaching ideal values. Near-ideal performance was demonstrated for continuous beam steering by optimization at angular increments of 0.5°. Inverse design moreover reduced the required phase modulation range for high beam directivity. High-directivity beam steering was reported for a phase modulation range as small as 180°. Furthermore, enhanced beam directivities using nonintuitive, inverse-designed array profiles were reported for an experimentally fabricated metasurface exhibiting a phase modulation of approximately 220°. Finally, a sensitivity analysis to antenna phase noise indicated that optimized designs could tolerate approximately ±30° phase error at each antenna without significant performance losses.

While the current work illustrates the power of an array-level inverse design on the beam steering performance in active metasurfaces, the same optimization framework can also be applied to a variety of alternative objective functions and active metasurface platforms. Similarly, a system-level optimization can also be performed for passive metasurfaces that rely on nonideal antenna components [97].

The results presented in this work constitute a compelling design approach for high performance in nonideal active metasurfaces. As an outlook, we expect that by combining array-level inverse design with optimization protocols applied to materials selection [98, 99], a modern era for co-design of materials, device and system is arriving for nanophotonics. Ultimately, such an approach will enable the realization of highly efficient multifunctional metasurfaces capable of many functions beyond beam steering.